JOURNAL OF GEOPHYSICAL RESEARCH, VOL. 96, NO. C12, PAGES 22,125–22,134, DECEMBER 15, 1991

Energy Density Directional Spectra of a Nearshore Wave Field Measured by Interferometric Synthetic Aperture Radar

M. MAROM, L. SHEMER,[1] AND E. B. THORNTON

Department of Oceanography, Naval Postgraduate School, Monterey, California

The nearshore wave field within Monterey Bay, California, is studied using remote sensing imaging by an interferometric synthetic aperture radar (INSAR) and simultaneous ground-based measurements. It is shown that INSAR imagery of the ocean surface offers some advantages over conventional synthetic aperture radar. Because of the direct imaging mechanism of INSAR, quantitative information about the complicated wave field can be obtained. The INSAR-derived directional energy density spectra and the corresponding ground-based spectra compare well.

1. INTRODUCTION

Oceanography has historically depended on sparse local measurements and observations made from ships and offshore stations. These observations yield the history of surface elevation and ocean current but are unable to provide the global spatial distributions of the measured quantities. The lack of a virtually instantaneous coverage of large ocean areas has limited our understanding of wave and current dynamics considerably.

The emergence of broad-spectrum (visible, IR, microwave) remote sensing techniques in the last decades offers methods capable of providing the desired information. In particular, considerable effort has been invested in the accumulation of experimental data using synthetic aperture radar (SAR) to image the ocean. SAR is a high-resolution coherent remote sensor carried either by an aircraft or by a satellite. The along-track (azimuthal) resolution of SAR is achieved by using the phase history of Doppler-shifted return signal over finite integration time. This Doppler shift is due to the relative velocity between the imaged ocean surface and the moving platform. The SAR imaging of the moving ocean surface is considerably more complicated than that of a stationary scene. The principles and related problems of SAR imaging of the ocean were surveyed by *Hasselmann et al.* [1985]. The results of the experimental and the theoretical studies of this technique, when applied to a moving surface, have shown that SAR has some limitations in imaging water waves. To a certain extent, the limitations of SAR with respect to ocean wave imaging are related to the lack of a well-defined imaging mechanism. The wavelike patterns visible in some SAR images of the ocean are attributed to different competing imaging mechanisms like tilting, hydrodynamic straining, and/or velocity bunching. As a result, wave spectra deduced from the SAR images can indicate only the wavelength and direction of the prevailing ocean wave systems and do not provide the absolute energy densities. In spite of these reservations, SAR remains one of the major tools in the study of ocean wave dynamics due to its unique potential of global coverage with high resolution.

Recently, *Goldstein and Zebker* [1987] suggested a modification of the conventional SAR by incorporating the interferometric principle. The basic technique consists of aligning two spatially separated antennas along the radar platform flight path. The backscattered echo obtained by each antenna is converted into a conventional complex SAR signal. The conventional SAR image is usually represented by the absolute value of this complex map produced by each antenna and constitutes the map of radar power reflectivity. In interferometric SAR (INSAR) processing, the two separate complex SAR images are combined into a single interferometric image. In contrast to the image intensity provided by the conventional SAR, INSAR image analysis uses the argument (phase) of the resulting complex value of each pixel, which is directly related to the local surface velocity. *Goldstein and Zebker* [1987] and *Goldstein et al.* [1989] have demonstrated the ability of the interferometric SAR to sense ocean currents.

In a preliminary report, *Marom et al.* [1990] have further developed the methods of applying INSAR to ocean wave measurements. They have shown that the major advantage of INSAR with respect to SAR is in the direct character of its imaging mechanism. The pixel intensity in an INSAR image is proportional to the line-of-sight surface velocity component and is not sensitive to the variation in radar backscatter cross section. Hence Marom et al. obtained clear patterns of wave systems in Monterey Bay using the INSAR technique, while in the simultaneously acquired conventional SAR images, also presented by Marom et al., waves could hardly be seen.

In the present work we study the wave field in the nearshore region of Monterey Bay using the INSAR images obtained from the flight paths with orthogonal directions, as well as simultaneously acquired surface-based information about the power and the directional wave spectra. It is demonstrated that INSAR is capable of providing quantitative data on ocean wave amplitudes and energy density directional spectra. By comparison of the wave spectra obtained by different means, the potential and limitations of this novel technique are analyzed.

2. THE EXPERIMENT

The experiment was carried out on September 8, 1989, in Monterey Bay. The site has a nearly uniform, albeit moderate, bottom slope (about 20 m/km) resulting in relatively

[1]Permanently at Department of Fluid Mechanics, Tel-Aviv University, Ramat-Aviv, Israel.

Paper number 91JC02222.
0148-0227/91/91JC-02222$05.00

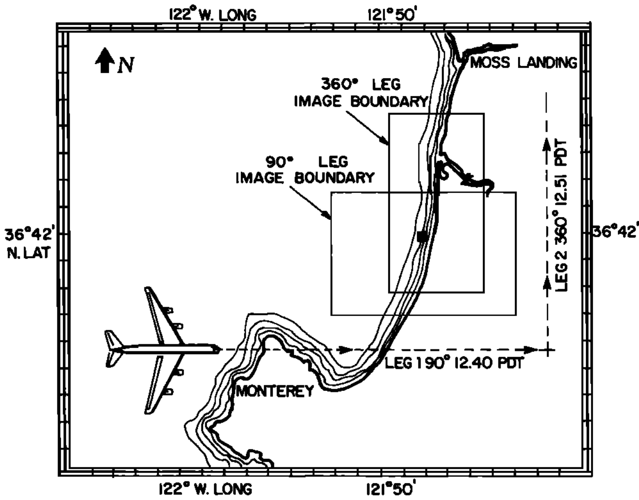

Fig. 1. Flight pattern and scene locations for INSAR data collection during the September 8, 1989, experiment off Marina, California. The solid square denotes the location of the shallow water pressure array.

small spatial regions required to meet the locally homogeneous bathymetry conditions necessary for the application of spectral analysis. The experiment consisted of four overflights of a NASA Jet Propulsion Laboratory (JPL) DC-8 airplane carrying an interferometric SAR. The present study reports only on the results obtained in the northern (360°) and eastern (90°) flight legs (Figure 1). The INSAR image boundaries included the location of a shallow water directional wave array offshore of the town of Marina. Radar data were acquired with the antenna beams aimed at the in situ wave array with a depression angle of 45° and mean altitude of 8250 m. The overflights were conducted around 1300 Pacific daylight saving time (PDT), close to the time of maximum tidal flood current. The scene locations of radar data and location of the directional wave array are illustrated in Figure 1. INSAR system and flight data are summarized in Table 1.

The environmental conditions during the experiment were typical for late summer in Monterey Bay. Light westerly winds (about 2 m/s), surface air temperature of 14°–16°C, and clear skies up to 300 m were observed. The mild meteorological conditions resulted in almost no local wave generation. The sea surface was predominantly long crested, narrow-band swell waves propagating shoreward. These conditions yielded an essentially linear modulation transfer function (MTF) of the ocean surface for imaging radars [cf. *Hasselmann et al.*, 1985].

The surface wind vector had mainly an eastward component with a weaker ambiguous northerly component. Thus in flight path 360°, the radar was looking at an upwind surface roughness, while in flight path 90° the radar looked at weakly cross-wind scenes. The resonant Bragg waves at the ocean surface which are responsible for the radar reflectivity traveled toward the aircraft on its 360° leg, but during flight path 90° they traveled both toward and away from the aircraft owing to wave and wind spreading.

TABLE 1. System and Flight Data for the Different Aerial DC-8 Aircraft Coverage During Marina Experiment, September 8, 1989

	90° Eastward Leg	270° Westward Leg	360° Northward Leg
Initial data collection time, PDT	1240	1301	1251
Aircraft velocity, m/s	214	216	214
Aircraft altitude, m	8285	8273	8178
Pulse repetition frequency, Hz	283	285	282
Near incidence angle, deg	17	nadir	nadir
Far incidence angle, deg	52.7	50.2	50.7
Ground pixel range spacing, m	8	7	6
Azimuth pixel spacing, m	12.1	12.1	12.1
Effective coverage range × azimuth, km^2	6 × 14	5.1 × 14	5.8 × 14

3. INSTRUMENTATION

The shallow water pressure gauge array is located at a depth of 16 m below mean sea level (MSL) off Marina Beach at 36°42'N, 121°48.9'W. The array consists of four piezoresistive pressure gauges in a square configuration, 6 m on a side, aligned 6° off true North. The pressure sensors are located 0.5–1 m above the bottom, while the northern sensor a Paroscientific, model 2100AS, digiquartz pressure sensor and the other three transducers manufactured by Kulite Semiconductor. Additional details about this directional wave array are given by *Seymour and Higgins* [1978]. The array was developed to provide wave directivity in shallow water. Time series records of consecutive 17.1 min of pressure data from all four channels (sensors) were processed for the required experimental period. These records were examined for data gaps and signal interference, and some of the relevant recognized errors were edited in the initial preprocessing by Scripps Institution of Oceanography, La Jolla, California.

An anemometer is located on Marina Beach at 36°42'N, 121°48.9'W. The anemometer is a 2102 Skyvane four-bladed, low-threshold impeller wind sensor mounted at an altitude of 27 m above MSL. The accuracy of wind speed measurement is 0.5 m/s for wind speeds less than 15 m/s. The wind direction is accurate to about 2°.

The NASA JPL DC-8 has a multifrequency, multipolarization airborne SAR system operating at L, C, and P bands with a full digital recording capability and an inertial navigator system for three-dimensional measurement of the aircraft attitude. Detailed parameters of the system are given in Table 2. At L and C bands the radar can operate in an along-track interferometer mode by using physically separated fore and aft antennas mounted on the left looking side of the aircraft fuselage. The spatial separation B between the antennas is 19.6 m. Additional details about the radar facility are described by *Held et al.* [1988].

In the present configuration, pulses are transmitted from the rear antenna and are received simultaneously by both antennas. The resulting signals are converted, separately, into two conventional complex SAR images [e.g., *Hasselmann et al.*, 1985]. The frequency ω of the backscattered radar signals at both antennas is Doppler shifted by an amount ω_D due to nonzero surface velocity vector $\mathbf{U}$. The frequency shift is given by

$$\omega_D = 2\mathbf{k} \cdot \mathbf{U} = 2kU_r, \qquad (1)$$

TABLE 2. NASA/JPL DC-8 Airborne Imaging Radar Parameters Employed During Marina Experiment, September 8, 1989

Parameter	L Band Value
Frequency, MHz	1237–1260
Center frequency, MHz	1248.75
Wavelength, cm	24
Chirp length, μs	11.25
PRF/V, Hz/m/s	1.32
Bandwidth, MHz	20
Peak power, kW	6
Azimuthal beamwidth, deg	8
Vertical beamwidth, deg	44
Antenna beam center gain, dB	18.3
Azimuthal pixel spacing, m	3.03 × 4
Slant range spacing, m	6.6
Polarization	VV
Receiver dynamic range, dB	30–56
Number of bits per sample	8
Number of looks	1
Available number of pixels, range × azimuth	750 × 1024

where $\mathbf{k}$ is the radar wave number vector and U_r is the radial component of $\mathbf{U}$. The velocity $\mathbf{U}$ represents the vector sum of surface currents, orbital velocity of the ocean waves, and the phase velocity of the resonant Bragg waves. For a platform moving with the velocity V, the image of the identical surface area by the two antennas is obtained with the time lag $\Delta t = B/2V$. The phase difference α between the return signals of the two INSAR antennas, which is due to the Doppler shift ω_D and the time interval Δt, is related to the measured radial component of the surface velocity U_r by:

$$\alpha = \omega_D \Delta t = \frac{kB}{V} U_r. \quad (2)$$

Equation (2), first obtained by *Goldstein et al.* [1989], serves as a basis for extracting the quantitative information from the INSAR images.

4. Data Acquisition and Processing

For each of the flight legs of this study, the complex image files of the same scene for each antenna have 750 range lines, with 1024 azimuth pixels in each line. The processed pixel spacings are approximately 7 m in the viewing (range) direction and 12 m in the azimuth direction. These complex images obtained by each of the two antennas are further combined to obtain separate INSAR images for phase and intensity. The interferogram is obtained by multiplying the complex value of each pixel in the image from the first antenna by the complex conjugate of the corresponding pixel in the second antenna image. The argument of the resulting complex number obtained for each pixel is the phase difference given by (2). Further, the effects of sideways aircraft movements, which were measured with the inertial navigation system, were subtracted from the interferogram, resulting in pixel phases which represent spatial ocean surface velocity fields only.

The raw image of 750 lines (in range direction) and 1024 pixels in each line (in azimuth direction) is linearly interpolated to obtain equal pixel spacing in both directions, in order to facilitate the subsequent Fourier analysis of the wave field. The phase difference can vary in the range $-\pi \leq \alpha < \pi$ and is represented in the INSAR image by 256 equally spaced pixel gray shades, so that the maximum positive (toward the observer) velocity with $\alpha = \pi$ corresponds to the pixel image value $N = 255$, negative velocity with $\alpha = -\pi$ corresponds to $N = 0$, and zero surface velocity (with $\alpha = 0$) corresponding to the $N = 128$. Thus using (2), the horizontal component of the surface velocity U_h for the incidence angle γ (measured from nadir) is given by

$$U_h = \frac{N - 128}{128} \frac{\lambda V}{2B \sin \gamma}, \quad (3)$$

where $\lambda = 2\pi/k$ is the radar wavelength.

Ground coordinates for each flight path were found by computing a best fit transformation between image and ground coordinates using a set of Global Positioning System (GPS) surveyed ground points visible in each SAR amplitude image of the solid surface region.

Because of the depth variations in the shallow water region in which the experiment was conducted, relatively small subscenes had to be selected from the overall image for spectral analysis. The selection of each subscene is based on satisfying both the assumption of constant depth and the minimum necessary size for Fourier analysis, which is approximately 6–10 wavelengths in each direction. When necessary, the selected subarea was zero padded to the nearest power of 2 number of pixels. The subscenes were demeaned and the edges cosine tapered to reduce spectral leakage.

5. Experimental Results

5.1. *INSAR Imagery of Nearshore Wave Field*

The INSAR phase images of the nearshore wave field obtained from the flight legs 360° and 90° are presented in Figures 2*a* and 2*b*, respectively. The rectangles in these images denote the subscenes which were subject to Fourier analysis. The images of Figure 2 clearly illustrate the difference between the stationary coast and moving water surface. This contrast is significantly enhanced as compared with conventional SAR images [cf. *Marom et al.*, 1990]. The image of the stationary coast is nearly uniform except for the Salinas River. The river is blocked off from the ocean at this time of the year and constitutes a relatively small basin of standing water, in which waves are generated only by local wind with no contamination by long fetch dominant waves and/or advecting currents. The apparent nonzero surface velocity in this basin, which manifested itself in the gray level different from the stationary surroundings, was measured and compared with Bragg phase velocity and wind direction. Anemometer measurements at the time of the radar airborne overflights show an eastward blowing wind of about 2 m/s, which indicates that for the 360° leg the radar was looking at upwind Bragg waves. The horizontal surface velocity U_h measured by INSAR in this case is equal to the phase velocity C_p of Bragg waves propagating in the viewing direction. The wave number k_B of the resonant reflecting waves is related to the radar wave number k and the local incidence angle γ through the Bragg condition [*Wright*, 1966]

$$k_B = 2k \sin \gamma, \quad (4)$$

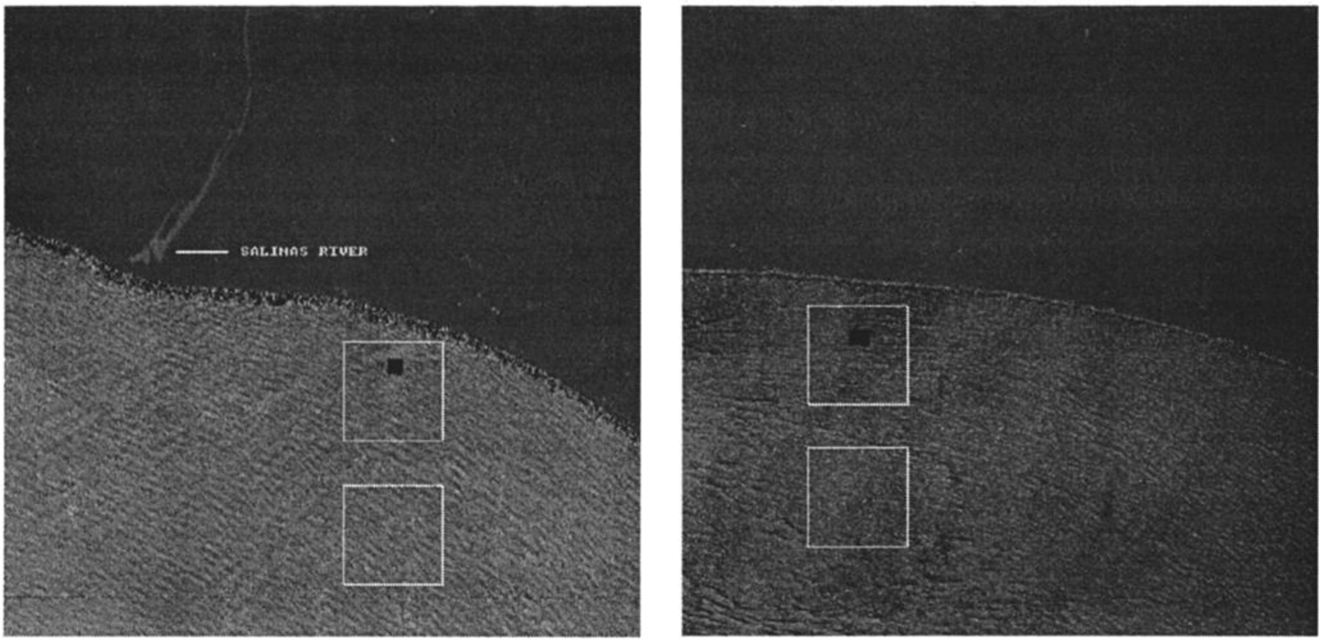

Fig. 2*a* Fig. 2*b*

Fig. 2. INSAR images of (*a*) northbound (360°) flight leg and (*b*) eastbound (90°) flight leg. Solid squares denote the location of the shallow water pressure array.

so that the phase velocity of Bragg waves calculated from the linear theory of deep gravity waves is

$$C_p = [g/(2k \sin \gamma)]^{1/2}. \qquad (5)$$

The mean incidence angle for the Salinas river image in Figure 2*a* is $\gamma = 46°$, resulting in the phase velocity $C_p = 51$ cm/s. The estimated horizontal velocity from the INSAR image of the Salinas river (Figure 2*a*), based on (2) and (3), is $U_h = 53 \pm 2$ cm/s, which is in good agreement with the theoretical Bragg wave phase velocity given by (5).

Shoaling and refraction of waves approaching the shore are clearly observed in both images of Figure 2. Two dominant swells with different wave lengths and propagating directions are visible in Figure 2*a* (360°). The longer swell propagating from west-southwest is more difficult to identify in Figure 2*b* (90°).

5.2. *Ground-Based Measurements*

The in situ wave array spectral results make possible independent verification of the INSAR measurements. Spectral analysis was performed on data collected at sampling frequency of 0.5Hz from 1200 to 1308 PDT on September 8, 1989. Fast Fourier transforms (FFTs) were computed for 128-s intervals and ensemble averaged. The resulting spectral estimates have approximately 64 degrees of freedom. The data were detrended and demeaned before being Fourier transformed to eliminate contamination of the spectra due to low frequency signals. The wave pressure power spectrum was calculated and transformed into surface elevation and surface slope spectra by applying linear wave theory transfer functions. The resulting spectra were subsequently converted from a frequency-angle presentation $S(\omega, \theta)$, where ω is the radian wave frequency and θ the wave propagation angle, to a two-dimensional wave number presentation $S(k_x, k_y)$. The computation of shallow water array directional spectra was done applying the exact Fourier coefficient representation method (V. Grauzinis, private communication, 1990), which is a modification of a method suggested by *Longuet-Higgins et al.* [1963] and allows for bimodal directional spectra. The technical details regarding the directional spectra computations are described by *Marom* [1990].

The directional wave spectrum resulting from these computations is presented in Figure 3. The spectrum is given in terms of wave numbers to facilitate comparison with the spatial INSAR-derived spectra. The wave numbers are calculated for the appropriate sensor depth (16 m) using the linear gravity wave dispersion relation. The two observed peaks in the spectrum correspond to wave periods of $T_1 = 15.9$ s and $T_2 = 9.1$ s. The shorter wave is much more smeared and is more energetic, with an amplitude which is higher by a factor of about 3 than that of the longer wave. It also appears to have a secondary peak at a wavelength

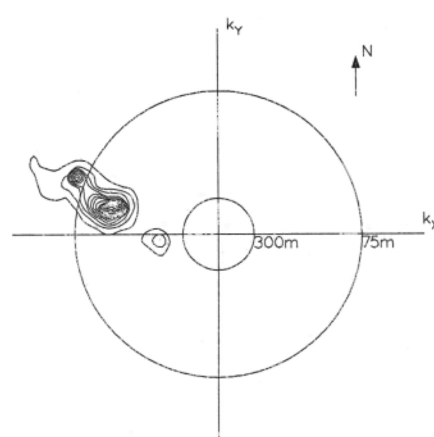

Fig. 3. The directional power spectrum obtained by the in situ shallow water pressure array.

TABLE 3. Actual INSAR Two-Dimensional Wave Number Wave Array Spectra Results and Predicted Refraction and Shoaling Data

		INSAR Two-Dimensional FFT				Predicted and Buoy Data				
Station	Mean Depth, m	L_1, m	α_1, deg	L_2, m	α_2, deg	L'_1, m	α'_1, deg	L'_2, m	α'_2, deg	Comments
1	16	96	291	192	256	98	283	192	260	L', α' measured by wave array
2	27	110	282	250	252	116	286	241	257	L', α' from model prediction
3	39	125	288	283	265	124	287	280	255	L', α from model prediction
4	52	135	301	310	264	127	288	306	253	L', α from model prediction

slightly below 75 m. The spectrum thus indicates the existence of two distinct swells. The shorter wave propagates from west-northwest to east-southeast, while the longer swell propagates from west-southwest to east-northeast. The wavelength and wave propagation direction estimates from Figure 3 are given in Table 3.

The directional wave spectrum $\mathbf{E}(\mathbf{k})$ can be described as a product of the omnidirectional power spectrum $E(k)$ and the angular distribution function $F(\theta)$. The surface elevation power spectrum $E(k)$ obtained by the wave sensors is illustrated in Figure 4*a*. The two wave systems from Figure 3 can be clearly identified in this presentation also. The dimensionless directional spreading functions $F(\theta)$ calculated from the directional spectrum of Figure 3 for these two swells are shown in Figure 4*b*. Note that the normalization is performed in radians, so that $\int_0^{2\pi} F(\theta)\, d\theta = 1$, but the propagation direction angles are marked in degrees for the sake of convenience. The $F(\theta)$ are presented for 80.2 m $< \lambda <$ 115.6 m and 180.7 m $< \lambda <$ 207.1 m bands, centered at the peaks of Figure 4*a*. The longer waves with a mean wavelength $\bar{\lambda}$ = 192.5 m, coming from west-southwest, most probably were generated by a late winter southern hemisphere storm occurring 8 days earlier and identified by weather maps to be located at 40°S to 60°S in the South Pacific. These southern swells are usually less energetic (smaller amplitude after traveling 10,000 km) and longer in period than swells originating in the North Pacific [*Snodgrass et al.*, 1966]. During late August and early September 1989 the normal high pressure system was deformed in shape and orientation by a series of low-pressure regions in the northwest Pacific. This storm appears to be the source of the more energetic and more dispersed northwesterly 9.1-s swell observed at Marina on September 8, 1989.

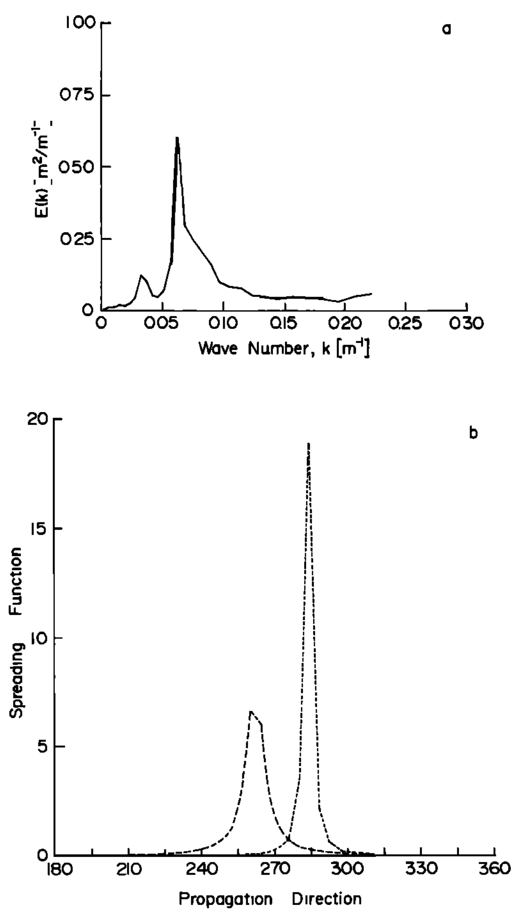

Fig. 4. (*a*) The surface elevation energy density spectrum from the pressure sensor measurements. (*b*) The angular distribution function from the shallow water pressure array, for 80.2 m $< \lambda <$ 115.6 m (short-dashed line) and 180.7 m $< \lambda <$ 207.1 m (long-dashed line).

5.3. *The INSAR-Derived Directional Spectra*

The wavelengths and propagation directions from the ground-based measurements can be compared with the estimates from the subareas marked in the INSAR images depicted in Figure 2. The ground-based pressure array is located inside the shoreward boxes in Figure 2. The two-dimensional wave number spectra are given in Figure 5*a* for the 360° flight leg, and in Figure 5*b* for the 90° leg. The 180° directional ambiguity, typical to spatial spectra derived from "snapshot" images, exists also in the INSAR spectra. This ambiguity is easily resolved in our case, however, since waves in the nearshore region can be assumed to propagate toward the beach. The spectrum in Figure 5*a* clearly shows two wave systems, quite similar to those observed in Figure 4. The wavelengths and the wave propagation directions corresponding to the local maxima in Figure 5*a* are also given in Table 3 and are in agreement with the surface-based estimates. The spectrum in Figure 5*a* does not show the presence of notable waves shorter than about 75 m, while these waves can be noticed in the ground-based spectrum of Figure 3. The considerably degraded image in Figure 2*b* affects the quality of the derived spectrum in Figure 5*b*. Still, the maximum in this spectrum corresponds to a wave with length λ = 102 m, propagating in the direction of 279°. This is in agreement with the short-swell parameters obtained from the 360° flight path, as well as from the pressure array. The less prominent longer swell, however, can not be distinctly identified in the spectrum.

The effects of refraction and shoaling due to the varying bathymetry can be seen by comparing the nearshore spectra of Figure 5 with those from the offshore boxes in Figure 2. The offshore spectra, corresponding to the areas with aver-

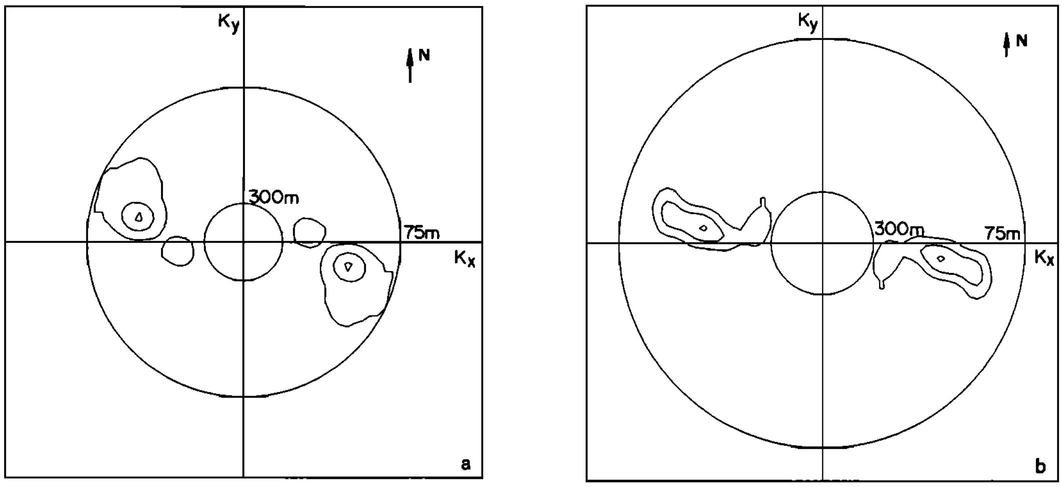

Fig. 5. The shallow water (mean depth h = 19 m) directional spectra derived from the INSAR images for (*a*) 360° and (*b*) 90° flight legs.

age depth of 39 m, are presented in Figure 6. In Figure 6*a* (flight direction 360°), both swell wave systems identified in the vicinity of the shallow water pressure array are clearly seen. Data on the corresponding wave lengths and propagation directions are also given in Table 3, where they are compared with the appropriate parameters calculated from the pressure array data using linear theory of refracting waves. The estimates of wave lengths and propagation directions from the INSAR spectrum of Figure 6*a* appear to be in agreement with the model predictions. Both wave systems now have longer wavelengths, and comparison of their angles of propagation at both locations indicates notable refraction. The same subarea in the INSAR image from the 90° flight path in Figure 2*b* also features a bimodal system (see Figure 6*b*). In this spectrum, however, no long-wave swell can be identified, as was the case with the nearshore spectrum of Figure 5*b*. In contrast to the previous case, an additional, shorter swell with the wave length of 116 m and propagation angle of 322° appears to be energetic here. This wave system is visible only in this particular location of the image and most probably is of local nature. The short swell also has a well-defined peak in the spectrum of Figure 6*b*. This peak corresponds to a wavelength of 131 m and propagation direction of 288°, again in agreement with both the 360° flight leg INSAR data and the model predictions.

In order to study the INSAR imagery of wave shoaling and refraction in greater detail, the two swell components observed by the shallow water array were used as inputs to compute wave ray traces using *Dobson*'s [1967] numerical model for linear refraction. The details of the ray trace computations are presented by *Marom* [1990]. Two-dimensional INSAR wave number spectra were computed from the INSAR image given in Figure 2*a* for subscenes along the ray traces. Rays at the peak frequencies (0.063, 0.109 Hz) were propagated offshore starting at the shallow water array. To reduce homogeneity constraints, two typical sizes of image subareas were selected for computing the two-dimensional wave number spectra. For the shorter wave field, subareas of about 1400 m × 700 m were selected for computing wavelength and direction, while for the long-crested swell, subareas of about 1400 m × 1400 m with overlap between the subareas were used. Table 3 gives the results of the two-dimensional wave number spectral analy-

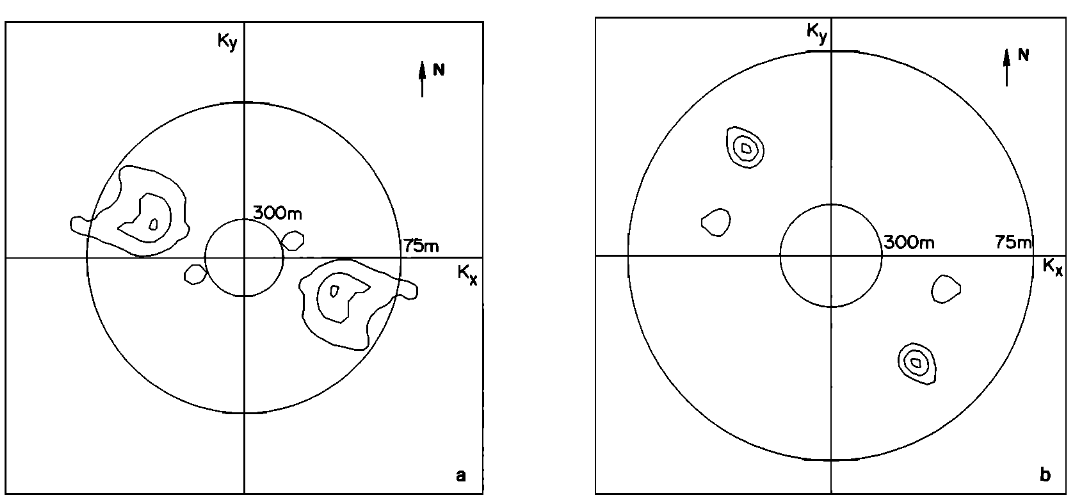

Fig. 6. As in Figure 5, but for mean water depth of 39 m.

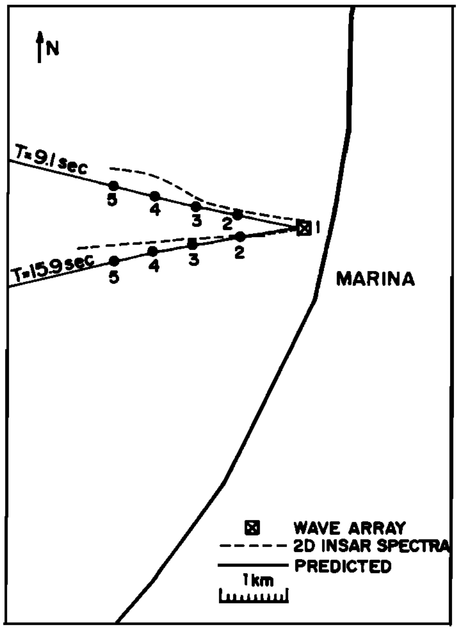

Fig. 7. The ray traces for the dominant swells originating at the shallow water pressure array. The solid line shows the linear model prediction; the dashed line shows the derivation from the INSAR spectra. The numbers denote the centers of two-dimensional FFT subareas.

sis of INSAR images along the ray traces as depicted in Figure 7. The agreement for the narrow-band long-crested swell is better probably because this swell is more monochromatic in character relative to the shorter swell, and hence more comparable to the theoretical model, which is based on the analysis of monochromatic waves as input. Wave propagation angles can be affected by oceanographic phenomena like tides and coastal currents. Wavelengths are also subject to these affects, but to a much lesser extent [*Shuchman and Kasischke*, 1981; *Hayes*, 1980]. These effects were not considered in our refraction model. The predicted wavelength and direction along the refracted ray (about every 800 m) were compared with the actual wavelength and direction of the two-dimensional INSAR image wave number spectra from the northern (360°) flight path image.

The refraction model becomes insensitive to changes in depth approximately when the water depth $h > 0.4\ L_0$, where L_0 is the deepwater wavelength. For the two observed swells in the Marina experiment, this requirement gives a depth of 54 m for the shorter swell (9.1 s) and 163 m for the longer swell. The western edges of the northern (360°) flight path INSAR image represents a mean depth of 53 m. This indicates that both wave trains experience shoaling and refraction through the entire imaged scene.

5.4. *INSAR-Based Energy Density Spectra*

The results reported in the preceding sections give confidence in the ability of INSAR to image ocean waves in a complex region under the given environmental conditions. Invoking (2), we now attempt to extract quantitative information about the wave amplitudes. The INSAR spectra in Figures 5 and 6 provide the two-dimensional wave number structure of the spatial distribution of the radial surface

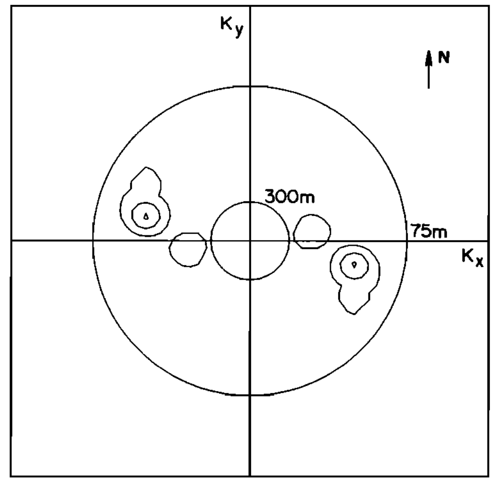

Fig. 8. The directional power spectrum of the surface elevation, derived from the INSAR spectrum of Figure 5*a*.

velocity component U_r. Since the contributions to U_r from both Bragg wave phase velocity and mean current can be assumed independent of spatial coordinates (at the length scales of the selected subscenes) and thus give only the dc component of the spectrum, ocean wave orbital velocities constitute the sole source of the spatially variable (ac) part of the wave number spectrum. In order to obtain the two-dimensional spectrum of the surface elevation to compare with the ground-based measurements, the radial velocity component spectrum has to be appropriately transformed.

It can be easily shown that for a given wave number $\mathbf{k} = (k_x, k_y)$, x being the radial direction, and with γ the radar beam incidence angle, the relation between the amplitude of the radial velocity $\hat{U}_r$ and the amplitude of the surface elevation $\hat{\eta}$ is given by

$$\hat{U}_r = \omega G(\gamma, \mathbf{k}, h)\hat{\eta}, \qquad (6)$$

where the frequency of the surface gravity waves ω is given by the linear dispersion relation

$$\omega = [kg \tanh (kh)]^{1/2} \qquad (7)$$

$$G(\gamma, \mathbf{k}, h) = \left[\left(\frac{k_x}{k \tanh (kh)}\right)^2 \sin^2 \gamma + \cos^2 \gamma\right]^{1/2}. \qquad (8)$$

It follows from (6) that in order to obtain the energy density at any given wave number $\mathbf{k}$, the corresponding value in the regular INSAR directional power spectrum has to be divided by the product $(\omega G)^2$. It can be seen from (7) and (8) that this procedure selectively amplifies longer waves and gives preference to azimuthally propagating waves. For that reason, low wave number noise, corresponding particularly to azimuthal waves longer than about 300 m, must be filtered out of the INSAR spectrum before this transformation is applied. The directional energy density spectrum of the surface elevation $E(\mathbf{k})$, calculated by such transformation procedure from the spectrum of Figure 5*a*, is given in Figure 8. The three contour levels shown in this Figure correspond to the power levels of 10, 30 and 50 in arbitrary units.

The quantitative comparison with the ground-based power spectrum of Figure 4*a* can be performed by integrating the

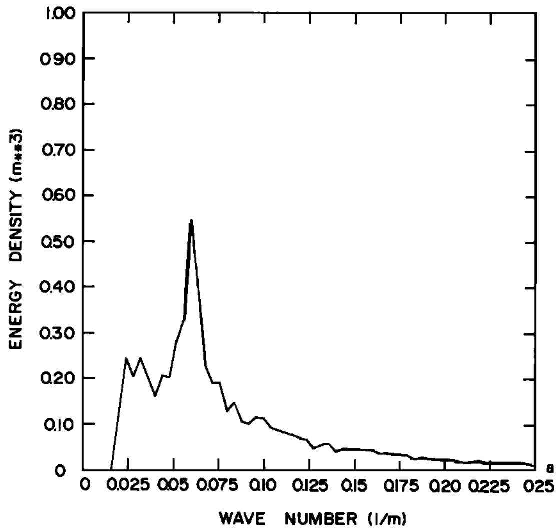

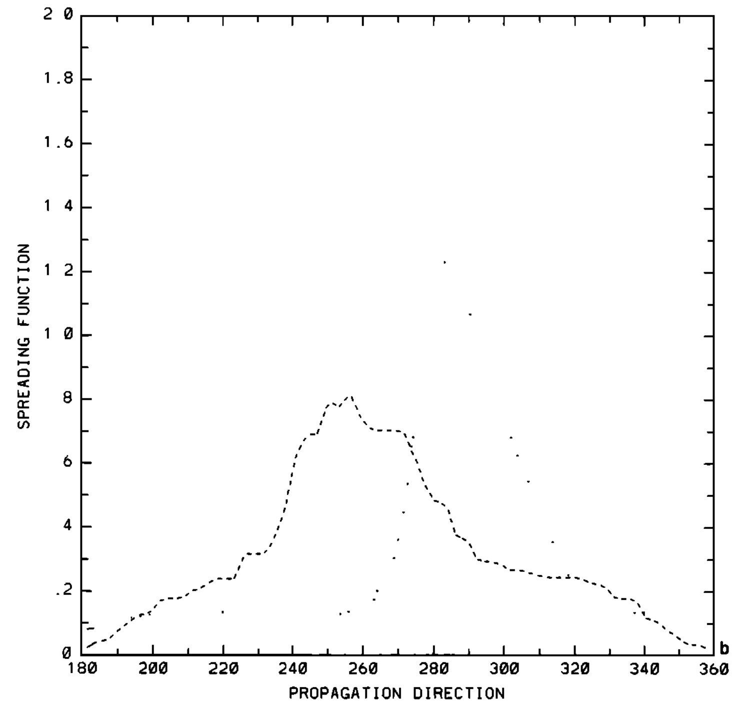

Fig. 9. The INSAR-derived (*a*) surface elevation power spectrum and (*b*) angular distribution function, for 85 m < λ < 110 m (dotted line) and 180 m < λ < 205 m (dashed line).

directional spectrum of Figure 8 over the propagation direction angles, which yields power spectrum $E(k)$ (Figure 9*a*). While the normalization procedure applied on the spectrum of Figure 4*a* does not affect the location of the maxima in the spectrum, the selective amplification of longer waves is obvious from comparison of Figures 5*a* and 8. One can see that both spectra are very similar, with the peaks of comparable height located at close wave numbers. Moreover, integrating the spectrum of Figure 9*a* with respect to the wave number k gives a total variance $\sigma^2 = 0.022$ m^2, corresponding to the significant wave height $H = 4\sigma = 0.60$ m. The variance of the spectrum in Figure 3 is $\sigma^2 = 0.021$ m^2, and the significant wave height $H = 0.58$ m.

The agreement between the INSAR-derived angular distribution function $F(\theta)$, normalized by the mean value (Figure 9*b*) and the corresponding ground-based directional spreading function (Figure 4*b*), is less impressive. $F(\theta)$ is obtained by integrating the INSAR-derived directional spectrum over the wave numbers for each wave propagation direction. The resulting angular distribution function for the shorter swell (center wavelength $\bar{\lambda} = 97$ m) in Figure 9*b* is similar to that of Figure 4*b*, although it is somewhat wider and has substantially lower peak value. The low peak value in Figure 9*b* compared with Figure 4*b* is a result of a higher level of noise in the INSAR-derived angular distribution function. For the longer swell, $\bar{\lambda} = 192.5$ m, angular distribution in Figure 9*b* again has the maximum at the propagation direction very close to that of Figure 4*b*. However, the angular distribution function for this wavelength is even more smeared, most probably as a result of the relative amplification of noise for the longer waves by equation (8) and poor resolution due to the limited sampling area. It is worth noting that while each INSAR image represents total sampling time of about 1 min, the ground-based results were obtained by acquisition of pressure gauge data over more than 1 hour. Some discrepancies between the results obtained by these different experimental techniques can be attributed to certain nonstationarities of the ocean wave field. It should also be stressed here that the INSAR spectra of Figures 5 and 6 are particularly noisy at low wave numbers, since the subareas analyzed are of the size of very few wavelengths. These results suggest that INSAR imagery of a more uniform wave field, for example, in the deep ocean where higher spectral resolution can be easily achieved, may be less noisy at the dominant length scales and thus less subject to the apparent broadening of the angular distribution function.

6. Discussion

The present experiments were performed in a nearshore region, with land constituting a sizable portion of each image. The presence of an area in the image with well-known surface velocity (zero velocity in this case) allows calibrating the system to an absolute velocity to reduce errors. The same procedure was employed in the pioneer INSAR studies by *Goldstein and Zebker* [1987] and *Goldstein et al.* [1989], which demonstrated that ocean currents can be accurately imaged by INSAR. The presence of a closed water reservoir (Salinas River) in the images of the current study allows comparison of INSAR measurements with actual observed phase velocity of the resonant Bragg waves [*Marom*, 1990; *Marom et al.*, 1990]. This additional indication of INSAR ability to measure accurately the absolute values of surface velocities is important at these initial stages to verify INSAR applications to the ocean studies in order to gain the necessary additional positive experience with this technique.

The nearshore region with varying bathymetry provided the opportunity to demonstrate the potential of INSAR in imaging a complicated shoaling and refracting wave field.

However, the price of studying shoaling wave fields is that small sample areas had to be chosen for spectral analysis, which necessarily imposed limitations on resolution. The experiment in a more homogeneous area, for example, the open sea, would be free of such limitations. The lack of known velocity reference under these conditions may make it difficult to verify the accuracy of the measured velocities. The knowledge of exact absolute velocities, however, is not essential for the analysis of ocean waves, since a constant nonzero offset does not affect the spatially variable part of the wave number spectrum. It thus appears that INSAR can be particularly effective in remote sensing of the dominant ocean wave systems over large areas.

All their differences notwithstanding, INSAR remains a modification of the conventional SAR and as such is subject to the same numerous phenomena that can degrade SAR resolution. The theoretical analysis of INSAR imagery of ocean which takes into account some of these phenomena was recently performed by *Shemer and Kit* [1991]. Careful analysis of the present data provides evidence of the effects of the finite width of the temporal correlation function of ocean reflectivity (scene coherence time τ_c [e.g., *Kasilingam and Shemdin*, 1988]). The finite value of τ_c results from random movement of the ocean surface at subresolution length scales. For τ_c much smaller than the processing integration time T, the azimuthal (along track) resolution l_{az} is degraded to [*Lyzenga and Shuchman*, 1983]

$$l_{az} \simeq \frac{\lambda R}{2V\tau_c}, \tag{9}$$

where the slant R is defined as the distance from the radar to the imaged point. The L band radar scene coherence time estimation during the Tower Ocean Wave and Radar Dependence experiment [*Plant and Keller*, 1983] is $O(10^2)$ ms. The preliminary results based on the present images give τ_c of the same order of magnitude [*Marom*, 1990]. It is clear from (9) that the degradation in azimuth resolution increases with increasing slant range R, so that the largest unresolvable azimuthally propagating waves can exceed 100 m in wavelength for large inclination angles.

The degradation in azimuthal resolution due to finite scene coherence time has a low-pass filter effect on SAR, as well as on INSAR, images. An example of this effect is inferred by comparing the wave array directional spectrum (Figure 3) and the corresponding INSAR-derived spectra (Figure 5). The wave array spectrum clearly shows another peak with a wavelength of 70 m and direction of 300°. For flight path 360° (Figure 5*a*) this wave is more azimuthally oriented (and hence more degraded) than the other two swells; therefore this swell is practically not seen in the 360° INSAR image spectrum.

The degradation in azimuth resolution may constitute a major reason for the less pronounced wave patterns in the INSAR images obtained from flight path 90°. The dominant swells in this image are more azimuth oriented, and therefore more degraded. It appears that the wave pattern in the INSAR image obtained from flight path 90° is less pronounced mostly owing to the azimuthal smear caused by the finite scene coherence time.

The 90° image in Figure 2*b* demonstrates the range dependence of the azimuthal resolution. At low incidence angles, where the degradation in azimuth resolution is relatively small, waves are clearly observed in the INSAR image. At higher incidence angles, with increased slant range and thus stronger degradation, the contrast of the image decreases, and the waves are less pronounced. This illustrates the important role of the finite scene coherence time in determining the capacity to image ocean surface waves.

Another effect which could contribute to the better quality of the 360° image is the azimuth image shift, usually called velocity bunching [*Swift and Wilson*, 1979; *Alpers and Rufenach*, 1979]. Velocity bunching is the distortion of SAR image due to spatial variation of the radial component of the orbital velocity. The image obtained from the 90° flight leg is more affected by this distortion mechanism. While for a conventional SAR, velocity bunching may serve as an important imaging mechanism, it seems that for the INSAR imagery it plays a negative role. The observed wave field for the 360° flight path contained mainly range-oriented waves. This orientation minimizes the effects of velocity bunching. The calculation of the velocity bunching parameters [*Alpers and Rufenach*, 1979] for all imaged waves in the Marina experiment indicates, however, that this effect was not dominant under the existing experimental conditions.

In addition to the degradation in azimuthal resolution due to the aforementioned effects, the SAR (and hence INSAR) azimuthal resolution is smeared also by the wave pattern translation and the range component of the surface acceleration during the finite integration time [*Alpers and Bruening*, 1986]. For a given wave system, the pattern translation smearing can be corrected by focus adjustment of the processing matched filter [*Lyzenga*, 1988; *Kasilingam and Shemdin*, 1988]. The smearing effects due to both acceleration and wave pattern translation were of minor importance under the present experimental conditions. An additional distortion mechanism results from the relative motion between the wave phase velocity C and the imaging radar platform velocity V [*Raney and Lowry*, 1978]. This so-called scanning distortion is proportional to the ratio C/V. Longer waves have higher phase velocity and hence are relatively more distorted. For this experiment, the scanning distortion even for the longer swell was within the spectral resolution error and thus also is disregarded.

7. CONCLUSIONS

The potential of using the interferometric SAR to measure ocean waves is demonstrated. The agreement between INSAR image spectra and in situ derived spectra is encouraging. In a sense, the similarity between the directional wave spectra obtained by a pressure array and those derived from the INSAR images can serve as a check for both these techniques.

The shoaling and refraction of a bimodal wave system was documented by INSAR and was found to be in agreement with the predictions of the linear wave refraction model.

It was shown that due to the direct imaging mechanism of INSAR, quantitative information about the wave amplitudes can be obtained from the images. The INSAR-derived estimate of the significant wave height and the wave number spectrum of the wave energy density were verified by the ground-based measurements.

The angular distribution function was measured experimentally for the dominant swells both by a pressure array and by processing the INSAR image. The agreement between the distribution functions obtained by both methods is quite satisfactory for the shorter swell, while for the longer swell it indicates a relative high noise level in the INSAR spectrum due to the spatial restrictions of the imaged scene.

The azimuth resolution is degraded for the finite scene coherence time. The importance of this effect on the actual performance of INSAR was demonstrated in the present study.

Acknowledgments. The authors are grateful to R. M. Goldstein of the Jet Propulsion Laboratory for providing the INSAR images and for his support and advice in the process of this study. This work was direct funded by the Naval Postgraduate School and supported by the Office of Naval Research. L.S. was supported by a senior research associateship from the National Research Council while visiting the Naval Postgraduate School.

REFERENCES

Alpers, W. R., and C. Bruening, On the relative importance of motion-related contributions to the SAR imagery mechanisms of ocean surface wave, *IEEE Trans. Geosci. Remote Sens., 66-24*, 873–885, 1986.

Alpers, W. R., and C. L. Rufenach, The effect of orbital motions on synthetic aperture radar imagery of ocean waves, *IEEE Trans. Antennas Propag., AP-27*, 685–690, 1979.

Dobson, R. S., Some applications of a digital computer to hydraulic engineering problems, *Tech. Rep. 80*, Stanford Univ., Stanford, Calif., 1967.

Goldstein, R. M., and H. A. Zebker, Interferometric radar measurements of ocean surface currents, *Nature, 328*, 707–709, 1987.

Goldstein, R. M., T. P. Barnett, and H. A. Zebker, Remote sensing of ocean currents, *Science, 246*, 1282–1285, 1989.

Hasselmann, K., R. K. Raney, W. J. Plant, W. Alpers, R. A. Shuchman, D. R. Lyzenga, C. L. Rufenach, and M. J. Tucker, Theory of synthetic aperture radar ocean imaging: A MARSEN view, *J. Geophys. Res., 90*, 4659–4686, 1985.

Hayes, J., Ocean current-wave interaction, *J. Geophys. Res., 85*, 5025–5031, 1980.

Held, D. N., W. E. Brown, A. Freeman, J. D. Klein, H. Zebker, T. Sato, T. Miller, Q. Nguyen, and Y. Lau, The NASA/JPL multifrequency, multipolarization airborne SAR system, Proc. IGARSS '88, *Eur. Space Agency Spec. Publ., SP-284*, 1988.

Kasilingam, D. P., and O. H. Shemdin, Theory for synthetic aperture radar imaging of the ocean surface: With application to the Tower Ocean Wave and Radar Dependence Experiment on focus, resolution, and wave height spectra, *J. Geophys. Res., 93*, 13,837–13,848, 1988.

Longuet-Higgins, M. S., D. E. Cartwright, and N. D. Smith, Observations of the directional spectrum of sea waves using the motions of a floating buoy, in *Ocean-Wave Spectra*, pp. 111–136, Prentice-Hall, Englewood Cliffs, N. J., 1963.

Lyzenga, D. R., An analytic representation of the synthetic aperture radar image spectrum for ocean waves, *J. Geophys. Res., 93*, 13,859–13,865, 1988.

Lyzenga, D. R., and R. A. Shuchman, Analysis of scatterer motion effects in MARSEN X band SAR imagery, *J. Geophys. Res., 88*, 9769–9775, 1983.

Marom, M., Interferometric synthetic aperture radar imaging of ocean surface currents and wavefields, Ph.D. thesis, Nav. Postgrad. Sch., Monterey, Calif., 1990.

Marom, M., R. M. Goldstein, E. B. Thornton, and L. Shemer, Remote sensing of ocean wave spectra by interferometric synthetic aperture radar, *Nature, 345*, 793–795, 1990.

Plant, W. J., and W. C. Keller, The two-scale radar wave probe and SAR imagery of the ocean, *J. Geophys. Res., 88*, 9776–9784, 1983.

Raney, R. K., and R. T. Lowry, Oceanic wave imagery and wave spectra distortions by synthetic aperture radar, in *Proceedings, 12th International Symposium on Remote Sensing of Environment, Manila, Philippines*, pp. 683–702, Environmental Research Institute of Michigan, Ann Arbor, 1978.

Seymour, R. J., and A. L. Higgins, Continuous estimation of longshore sand transport, paper presented at Symposium on Technological, Environmental, Socioeconomic and Regulatory Aspects of Coastal Zone Management, Am. Soc. of Civ. Eng., San Francisco, Calif., 1978.

Shemer, L., and E. Kit, Simulation of an interferometric SAR imagery of an ocean system consisting of a current and a monochromatic wave, *J. Geophys. Res., 96*, 22,063–22,073, 1991.

Shuchman, R. A., and E. S. Kasischke, Refraction of coastal ocean waves, in *Spaceborne Synthetic Aperture Radar for Oceanography*, edited by R. C. Beal, P. S. DeLeonibus, and I. Katz, pp. 128–135, Johns Hopkins University Press, Baltimore, Md., 1981.

Snodgrass, D., G. W. Groves, K. F. Hasselmann, G. R. Miller, W. H. Munk, and W. H. Powers, Propagation of ocean swell across the Pacific, *Philos. Trans. R. Soc. London, Ser. A, 259*, 431–497, 1966.

Swift, C. T., and L. R. Wilson, Synthetic aperture radar imaging of moving ocean waves, *IEEE Trans. Antennas Propag., AP-27*, 725–729, 1979.

Wright, J. W., Backscattering from capillary waves with application to sea clutter, *IEEE Trans. Antennas Propag., AP-14*, 725–729, 1966.

M. Marom and E. B. Thornton, Department of Oceanography, Naval Postgraduate School, Monterey, CA 93943.

L. Shemer, Department of Fluid Mechanics, Tel-Aviv University, Ramat-Aviv 69978, Israel.

(Received July 22, 1991;
revised August 26, 1991;
accepted August 26, 1991.)